Channel Defect Detection in Food Packages Using Integrated Backscatter Ultrasound Imaging

Kay Raum, Ayhan Ozguler, Scott A. Morris, and William D. O'Brien, Jr., *Fellow, IEEE*

***Abstract*—Hermetically-sealed flexible food packages require very effective seal integrity testing to extend the shelf stability of thermally processed food. The initial goal of this study was to estimate the detection limits of laboratory-generated channels which simulate defects in food packages using pulse-echo ultrasonic imaging techniques. Packages with well characterized (*via* transmission optical microscopy) laboratory-generated channels that simulate defects with diameters between 9 and 325 μm in the seal plane traversing the major axis of the heat seal were generated in heat-sealed microwavable retort-pouch plastic film (trilaminate). Pulse-echo techniques in the 13–17 MHz center frequency range were investigated. The samples were examined with a conventional B-mode imaging technique, which was found to be inadequate for subwavelength imaging of the types of typical channel defects found in shelf-stable food packages. Based on conventional B-mode image features, a new goal of this study was established to develop and evaluate an imaging technique which would exhibit subwavelength imaging capabilities. The new imaging technique called backscattered amplitude integral (BAI) is introduced here. It was observed that BAI-mode imaging has the ability for subwavelength detection of channel defects, e.g., detection of a 10-μm diameter channel defect at a center frequency of 13.1 MHz ($\lambda = 182$ μm).**

I. Introduction

Retort pouches and trays are constructed of polymeric laminates and coextrusions, with little or no metallic content [at most, an extremely thin (< 25 μm) foil layer laminated in the interior of the material]. They are hermetically sealed and may be flexible pouches or semirigid trays sealed with a laminated film. These new types of packages offer a combination of the advantages of metal cans, microwaveable trays, and boil-in bags [1], [2]. For both the consumer and the manufacturer, preservation of the food product in retort pouches and trays has many advantages over canning or freezing. Some of these are improved food quality and reduced energy consumption through reduced thermal processing requirements as well as concurrent energy savings through the products' life-cycle [3], [4], on-line package forming, increased material efficiencies, ease of access to product, and faster heating of product via boiling or microwaving. As with all shelf-stable thermally processed foods, the integrity of the package is vital to human safety and product quality. Retort pouches have a fusion weld of two comparable polymeric film surfaces, and the integrity of these seals is central to the utility and safety of the package and product.

Currently 9CFR§381.301(d) [5] requires that producers manually inspect each container, once after the post-fill sealing and again after thermal treatment in a steam retort. The most common types of compromised seals involve a seal which has wrinkled or failed to seal or has included a foreign material. In most cases, the two layers of material are not torn or otherwise broken, but the fusion seal has been contaminated or has not been properly formed. In extreme cases, the void may be much larger than the combined thicknesses of the materials, because the opened section in the fusion seal can be as large as the seal area itself. Additionally, a seal with an incomplete seal may pass existing fusion tests (if applicable), but fail later during handling and shipping [6].

Four main methods of testing seal performance have been defined [6], viz., fusion testing, burst testing, tensile testing, and visual examination. Fusion, burst, and tensile test methods cannot detect any microleaks which are not clearly visible to the naked eye (< 50 μm in diameter) [6], [7]. Microchannels as small as 17 μm in diameter have been detected by using a helium leak test though the technique is slow (> 30 min) and spatially imprecise [8]. Moreover, few if any of these methods can detect a leak plugged with food, which may provide a path for microorganisms to "grow through" the seal. The food processing industry commonly uses destructive testing such as burst testing to perform spot checks of materials and sealing equipment, but an on-line, nondestructive inspection method is necessary to supplant the costly and inefficient manual inspection which restrict economical use of these packages.

Many of the current nondestructive methods available for inspection of materials have been evaluated [7]. These techniques included simple ultrasound (using a simple, low resolution, transmission method to measure large-scale seal formation without imaging capability [9]), ultrasound

Manuscript received June 3, 1996; accepted July 14, 1997. This work was supported in part by the Value-Added Research Opportunities Program, Agricultural Experiment Station, University of Illinois.

K. Raum is with the Institute of Medical Physics and Biophysics, Martin-Luther-University Halle-Wittenberg, D-06097 Halle/Saale, Germany.

A. Ozguler is with the Department of Food Science and Human Nutrition, University of Illinois, Urbana, IL 61801.

S. A. Morris is with the Department of Food Science and Human Nutrition and the Department of Agricultural Engineering, University of Illinois, Urbana, IL 61801.

W. D. O'Brien, Jr. is with the Bioacoustics Research Laboratory, Department of Electrical and Computer Engineering, University of Illinois, Urbana, IL 61801 (e-mail: wdo@uiuc.edu).

imaging (Scanning Laser Acoustic Microscopy), machine vision imaging, infrared imaging, infrared laser/fiber optic array, capacitance, spectrophotometer, X-ray, eddy current probe, and magnetic resonance imaging (MRI). Optical machine vision will detect only surface artifacts of defects and inclusons in the heat seal, and not the defect or inclusion itself. X-ray and MRI techniques can identify actual defects smaller than 50 μm, but both techniques have significant disadvantages. X-ray imaging does not detect the fusion seal in the polymeric materials, and X-ray measurements' need for imaging contrast require the microleak in the seal to contain only materials with markedly higher electron density than the hydrocarbons of the package, as well as the water and carbohydrates of the food in the package (because there are still two layers of intact material in the image), and thus it cannot detect an air- or product-filled channel. MRI cannot detect empty channels and has insufficient resolution and imaging speed.

Microbiological tests have attempted to quantify the approximate minimum size of a critical defect [7], [10]–[12]. The minimum leak size through which a microorganism might penetrate was shown to be 33 μm in diameter; however, this technique is still unreliable because 10% of pierced pouches which have the same defect size failed to show contamination. Other data about the minimum diameter of the microleak which permit microbial penetration are still inconclusive and quite variable. Defect sizes between 0.2 and 80 μm in diameter for bacterial penetration have been summarized, and the most common size was presumed to be around 10 μm [7]. In addition, the incubation period of test microorganisms is quite lengthy, making this on-line inspection technique impractical (although it is common manufacturing practice to hold finished lots of filled packages for a period of time and to inspect for swelling or other signs of failure). Simple measurement of the microorganisms yield little useful data because it does not consider means of transport and effects of secondary factors such as fluid surface tension and viscosity.

A recent study [13] using a scanning laser acoustic microscope (SLAM) operating at 100 MHz showed that channel defects as small as 10 μm in diameter can be detected. However, for transmission-mode imaging, the inspected sample has to be placed between the transmitting and receiving components of the system, which is not practical for many industrial applications due to the variety of different shapes of food packages. For the high frequencies required to detect 10-μm diameter defects, the insertion loss may be too great, thus further limiting the method to very thin samples. For example, at 100 MHz, the amplitude attenuation coefficients for commercially available polyethylene film (Ziploc® brand, DowBrands L. P., Indianapolis, IN) and plastic microwaveable retort pouch material (Fuji Tokushu Shigyo Co. Ltd., Seto Aichi, Japan) are 58 and 90 dB/mm, respectively [13]. High-frequency transmission technology, therefore, may have only limited application for the detection of defects in food packages. For lower-frequency pulse-echo technology, the sample has to be probed from one side only, and thick materials can be inspected if the area of interest is located close ($\approx$ 1 mm) to the surface, making it ideal for imaging film-film and film-molding seals from the film side.

In this study, laboratory-generated channel defects in the range from 9 to 325 μm in diameter in transparent plastic film with a total thickness of about 220 μm were used to evaluate relatively low-frequency pulse-echo imaging capabilities for defect detection. A new technique called BAI-mode imaging is introduced for the detection of defects. The BAI-mode imaging technique was found to be superior to conventional B-mode imaging for this application.

II. Sample Preparation and Validation

Thirty-four samples with laboratory-generated channel defects based on actual defect shapes and sizes known to lead to contamination of food within retort pouches were prepared. The channels were filled with either air or water in order to simulate high or low contrast cases, respectively; these are typical acoustic properties of channel defect materials. Microwaveable retort trilaminate pouches were used as a packaging material (Fuji Tokushu Shigyo Co., Ltd., Seto Aichi, Japan). The average propagation speed in the plastic trilaminate had been previously measured (2380 m/s [13]) and found to be in reasonable agreement with literature propagation speed values for the three individual materials, that is, 2600 m/s for oriented nylon [14], 2380 m/s for polyvinylidene chloride (PVDC) [15] and 2660 m/s for polypropylene [14]. This material is used commercially in Japan and was chosen for this study because it is optically transparent to allow for independent channel defect verification; generally the retort pouch can contain an aluminum layer or the surface of the package might be printed, thus rendering it opaque.

Each channel defect sample was prepared by placing a smooth, sapphire-die-drawn tungsten wire (10, 25, 37, 50, 75, 100 or 220 μm; California Fine Wire Company, Grover City, CA) between two layers of the trilaminate [Fig. 1(a)]. An automatic heat sealer (Doboy HS-C42051, Doboy Co., New Richmond, WI) was used to seal the tungsten wire into place at a sealing temperature of 132°C. After 5 minutes the wire was axially removed. The wire was removed with the sample either submersed in a water bath in order to fill the channel with water, or in air. Both ends of the channel were then fused to contain the contents within the formed channel. Optical micrsocopy was used as an independent check of the channel contents, especially for those channels smaller than 50 μm in diameter.

Visible small needle pricks were placed on opposing sides of the channel as reference marks [Fig. 1(b)] for both the ultrasound images and the light transmission microscope validation images.

Light transmission microscope images with a calibration grid (Reichert Jung: 2 mm divisions into subdivisions of 10 μm) were used to determine the exact cross-sectional channel defect dimensions (Fig. 2). Images were captured using a Nikon Optiphot-2 light microscope, Sony CCD

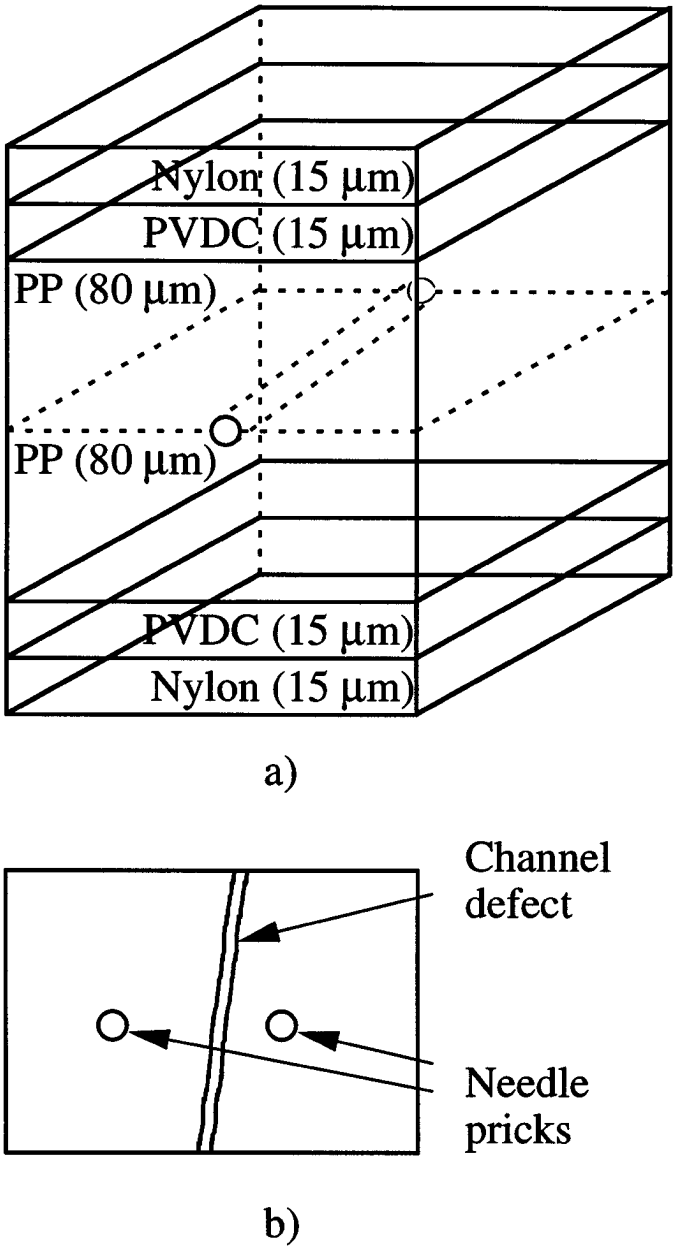

Fig. 1. (a) Three-dimensional, cut-away representation of two layers of the trilaminate retort pouch material with a channel defect shown schematically between the two layers, and (b) schematic top view. An individual trilaminate consists of three layers, viz., oriented nylon, polyvinylidene chloride (PVDC), and polypropylene (PP).

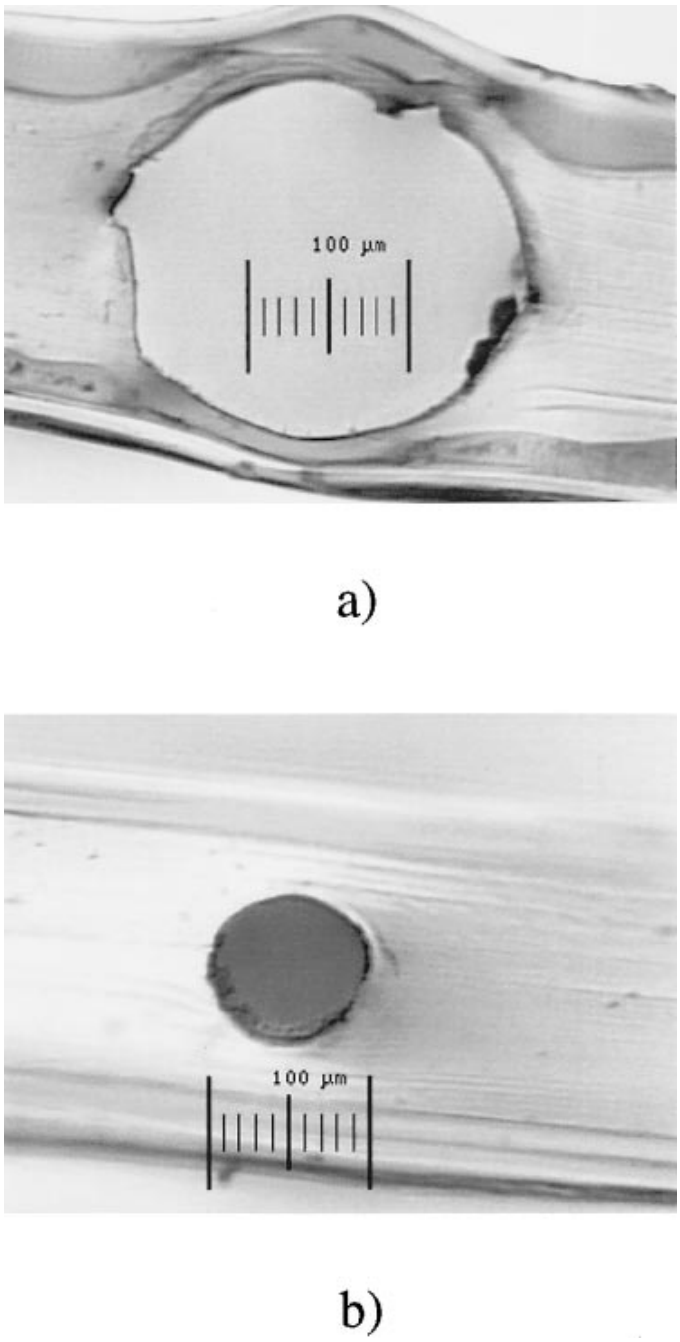

Fig. 2. Cross-sectional optical microscope images of water-filled channels with (a) 220-μm and (b) 95-μm channel diameters.

color video camera, RasterOps frame-grabber board, Macintosh IIci computer, and Adobe Photoshop software. The image area was 420 by 316 μm for the cross-sectional images and 2.1 by 1.6 mm for the top-view images, respectively. The cross-sectional channel shape was elliptical for all channel defects with the ellipse's major and minor axes generally parallel and perpendicular, respectively, to the plastic trilaminate surfaces. For definition purposes, the ellipse's major axis is the value quoted herein for the channel's diameter, that is, the dimension yielded from the top view. The defect dimensions were in a range from 9 to 325 μm in diameter and for channel diameters less than about 100 μm, the major axis to minor axis ratio ranged between 0.97 and 1.44. For channel diameters greater than 100 μm, this ratio had a greater range because delamination and distortion of the trilaminate structure occurred, presumably due to the wire removal process of the larger wire diameters.

These samples were prepared as a simple-case test of the imaging capabilities of the method. Real-world defects would potentially have much different paths and geometries, but it is surmised that the elliptical configuration of the simulated defects are the shortest path length with the least number of obstructions to microbial penetration,

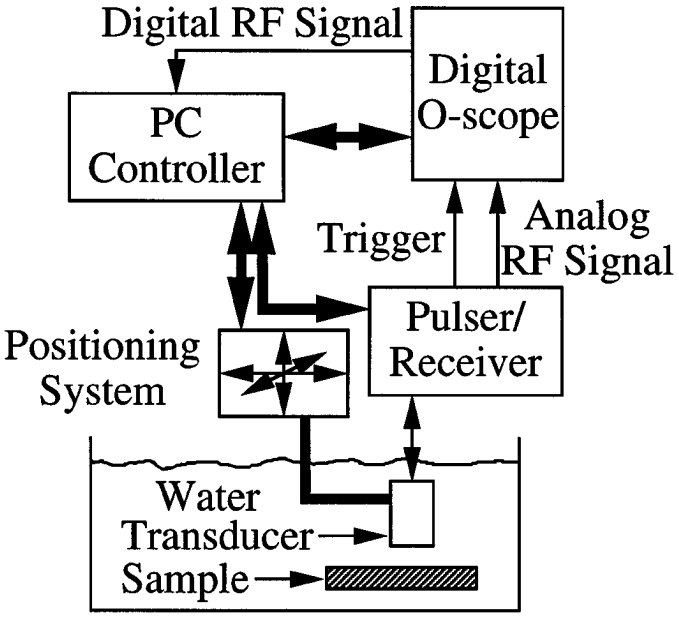

Fig. 3. System block diagram. The bold lines with arrows at both ends designate GPIB connections.

and therefore a worthwhile "worst case" model. Deformation of the channel cross-section due to the surface shear force imparted as the wire is withdrawn appears (from optical and confocal microscopy assessment of cross sections) to be minimal.

III. System Description and Characteristics and Data Acquisition

Fig. 3 shows the block diagram of the main system components. The channel-defect sample was placed in a water tank ($\approx$ 20°C) with the defect oriented approximately normal to the sound beam direction, that is, a top view [Fig. 1(b)]. Spherically focused ultrasonic transducers with manufacturer-quoted center frequencies of 15 and 20 MHz (Panametrics V319 and V317, respectively, Waltham, MA) were shock excited by a 300-V pulse produced by a computer-controlled pulser/receiver (Model 5800, Panametrics, Waltham, MA). The received echo signal was amplified (20 dB) and band-pass filtered (1 to 35 MHz) by the pulser/receiver, and then displayed (500 Ms/s) on a digitizing oscilloscope (Tektronix Model 11401) with a 10-bit resolution.

The measured transmit-receive spatial characteristics of the two transducers were in general agreement with the manufacturer's specifications [16]. The lateral acoustic pressure distribution in the focal plane of a spherical focusing source is described by [17], [18]:

$$\left|\frac{p(r)}{p(0)}\right| = \left|\frac{2J_1\left(\frac{kDr}{2\mathrm{ROC}}\right)}{\frac{kDr}{2\mathrm{ROC}}}\right| \tag{1}$$

where $p(r)$ is the peak acoustic pressure as a function of the off-axis lateral distance r, $p(0)$ is the on-axis peak acoustic pressure at $z = \mathrm{ROC}$, k is the wave number, D is the transducer's diameter and ROC is the transducer's radius of curvature where ROC also is considered the focal length at the geometrical focus; the true focus (maximum axial intensity location) is located closer to the transducer ($z <$ ROC) due to diffraction effects. $J_1(x)$ is a Bessel function of the first kind of order one. From (1) the −6-dB transmit-receive beam width (diameter) in the geometrical focal plane ($z = \mathrm{ROC}$) is:

$$D_{\mathrm{lateral\ (-6dB)}} = 1.028 \cdot \lambda \cdot f^{\#} \tag{2}$$

where $f^{\#}$ is the *f-number* ($= \mathrm{ROC}/D$) and λ is the acoustic wavelength ($= c/f_c$) where f_c is the ultrasonic center frequency. The experimental assessment of the lateral resolution was made in the true focal plane; the experimentally determined focal length (denoted F) was assumed to be equal to the ROC. This is a reasonable assumption for the strongly focused spherical sources used herein.

The axial acoustic pressure distribution of a spherical focusing source is described by [17], [18]:

$$\left|\frac{p(z)}{p(0)}\right| = \frac{\mathrm{ROC}}{z}\left|\mathrm{sinc}\left(\frac{D^2}{8\lambda\mathrm{ROC}}\left(\frac{\mathrm{ROC}}{z}-1\right)\right)\right| \tag{3}$$

where $p(z)$ is the peak acoustic pressure as a function of the axial distance z and $\mathrm{sinc}(x)$ is defined as $\frac{\sin(\pi x)}{\pi x}$. From (3) the approximate −6-dB transmit-receive depth of focus is:

$$F_z = 7.08 \cdot \lambda \cdot f^{\#^2}. \tag{4}$$

The pulse duration ($\tau_{(-20\mathrm{dB})}$) is defined as the time duration between the times when the pulse amplitude is at −20 dB of its maximum values. From the spatial extent of the pulse duration, the axial resolution is:

$$D_{\mathrm{axial}} = \frac{c \cdot \tau_{(-20\mathrm{dB})}}{2}. \tag{5}$$

The measured transmit-receive spectral characteristics of the two transducers yielded estimated center frequencies at slight variance with the manufacturer's quoted center frequencies. Fig. 4 (solid line) shows an RF acquired pulse-echo signal from the 20-MHz transducer. The pulser/receiver used in this study appeared to attenuate the higher frequency components, which resulted in the estimated center frequencies in the focal plane for the two transducers to be lower than the manufacturer-quoted frequencies, that is, 13.1 MHz for the 15-MHz transducer and 17.3 MHz for the 20-MHz transducer. Also assessed were the transducer's pulse-echo −6-dB bandwidths and fractional bandwidths, that is, respectively, 11.1–15.1 MHz and 30.7% for the 15-MHz transducer and 13.7–21.0 MHz and 42.4% for the 20-MHz transducer.

Table I gives an overview of measured and calculated acoustic field properties and resolution limits for the two transducers used in this study. The beam quantities were experimentally obtained using a 25-μm tungsten wire target [16]. Fig. 5 compares the calculated axial and lateral

TABLE I
MEASURED AND CALCULATED ACOUSTIC FIELD PROPERTIES AND RESOLUTION LIMITS.

Transducer or field quantity	V319 15-MHz Transducer	V317 20-MHz Transducer
*Source diameter, D	12.7 mm	6.35 mm
*Focal length, F	19.05 mm	12.70 mm
Measured focal length (water, 20°C), F	18.70 mm	12.44 mm
**f-number*	1.5	2.0
Measured center frequency (water, 20°C), f_c	13.1 MHz	17.3 MHz
Measured pulse duration (water, 20°C), $\tau_{(-20\ \mathrm{dB})}$	250 ns	155 ns
Calculated wavelength (water, 20°C), λ_{water}	113 μm	86 μm
Calculated wavelength (plastic, 20°C), $\lambda_{\mathrm{plastic}}$	182 μm	138 μm
Calculated axial resolution [(5) in water, 20°C], D_{axial} (using measured $\tau_{(-20\ \mathrm{dB})}$)	185 μm	115 μm
Calculated axial resolution [(5) in plastic, 20°C], D_{axial} (using measured $\tau_{(-20\ \mathrm{dB})}$)	298 μm	184 μm
Measured lateral resolution (water, 20°C), $D_{\mathrm{lateral}\ (-6\ \mathrm{dB})}$	187 μm	173 μm
Calculated lateral resolution [(2) in water, 20°C], $D_{\mathrm{lateral}\ (-6\ \mathrm{dB})}$	174 μm	177 μm
Measured depth of focus (water, 20°C), F_z	1800 μm	2150 μm
Calculated depth of focus [(4) in water, 20°C], F_z	1800 μm	2436 μm

*Denotes provided by manufacturer.
Propagation speeds at 20°C: $c_{\mathrm{plastic}} = 2380$ m/s [13], $c_{\mathrm{water}} = 1483$ m/s [21].

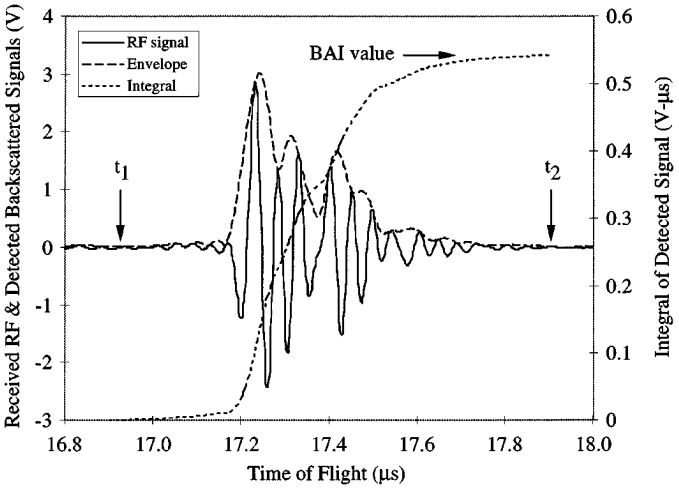

Fig. 4. A 17.3-MHz, RF signal, and the absolute value of the Hilbert-transformed signal (envelope) from an undisturbed region of the trilaminate plastic retort of thickness 220 μm. The integration boundaries for envelope (right-hand axis) to determine the BAI value are between t_1 and t_2 and, for this RF signal, the BAI value is 0.543 V-μs.

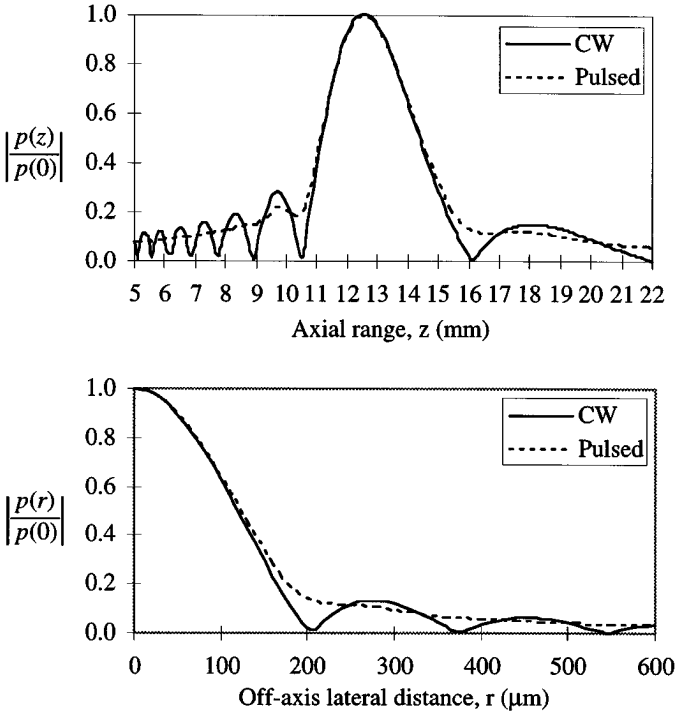

Fig. 5. Calculated axial (top) and off-axis lateral (bottom) distributions at the axial maximum distance for CW (17.3 MHz) and pulsed (spectrum obtained from the 20-MHz transducer) conditions.

beam distributions [(3) and (1), respectively] under CW (17.3 MHz) and pulsed (spectrum obtained from the 20-MHz transducer—see Fig. 4) conditions, and demonstrates that the respective distributions are similar in the focal region. For pulsed-wave conditions used herein, the distributions beyond the focal region are relatively smooth compared to the CW distributions.

The image data were acquired by moving the transducer relative to the fixed-position sample in a rectangular grid pattern with a computer-controlled micro-precision positioning system (Daedal Inc., Harrison City, PA) which has a linear positional accuracy of about 2 μm and a rotational accuracy of about 0.02°. The angle of incidence of the ultrasound beam was intentionally oriented at a known angle either normal or slightly oblique ($\leq 10°$) to the plane of the plastic surface (small wrinkles in the surface were neglected). The positioning system, oscilloscope, and pulser/receiver were connected to a GPIB-board and controlled by a 486-66 PC. The grid spacings in the direction parallel to the channel's major axis (channel's diameter) was 30 μm and in the direction parallel to the long axis of the channel defect was 100 μm, thus yielding, respec-

tively, with the step sequence of 100 by 40 used for the "in-plane" scan, a 3-mm by 4-mm field of view. The number of RF data acquisitions per data set was 4000 (100 by 40). This three-dimensional data set containing all 4000 512-point RF data acquisitions was stored to the PC's hard disk and transferred to a SUN Sparc 20 workstation for off-line processing. All computations were performed with MATLAB® software (The MathWorks, Inc., Natick, MA).

The B-mode images were processed from one row of each acquired RF data acquisition, where, as seen in Fig. 6, the row was perpendicular to the channel's long axis, that is, the plane of the B-mode image cut across the channel defect. Each RF data acquisition was filtered using a 400th order Remez-bandpass filter (3 to 27 MHz cutoff frequencies) and envelop detected using the absolute value of the Hilbert-transformed, filtered RF signal. The built-in MATLAB® function was used to process the Hilbert-transformation. The detected signal was linearly interpolated in the lateral direction by a factor of two to yield the lateral pixel dimension of 15 μm. The axial dimension was determined from

$$z(t) = \frac{c \cdot \mathrm{TOF}}{2} \tag{6}$$

where c is the measured plastic propagation speed (2380 m/s [13]) and TOF is time of flight. The axial pixel dimension was 2.38 μm, which corresponds to a 2 ns TOF.

IV. BAI-Mode Imaging

The motivation for developing a different imaging procedure was prompted by results and observations from the B-mode images (two-dimensional image plane parallel to the direction of the transmitted ultrasonic signal path). Theoretical considerations and experimental findings demonstrated that resolution limited conventional B- or C-mode image detection for channel defects less than the acoustic wavelength (see discussion below). For normal-incidence 17.3-MHz B-mode images of water-filled channels, the defect was approximately resolved for the 220-μm diameter channel, but was not resolved for the 95-μm diameter channel (Fig. 6). However, a characteristic shadow at the location beyond (posterior to) the expected channel location was observed, as is seen in the 95-μm channel defect B-mode image. Also, this characteristic shadow resulted in the absence of the echo from the bottom water-plastic surface immediately posterior to the channel location. The characteristic shadow region in the normal-incidence B-mode images suggested that any discontinuity in the plastic layer could affect the received RF echo signal and possibly the total reflected echo energy. A means to quantify the reflected RF echo signal (solid line in Fig. 4) is to integrate the detected signal (the absolute value of the unfiltered Hilbert-transformed RF data

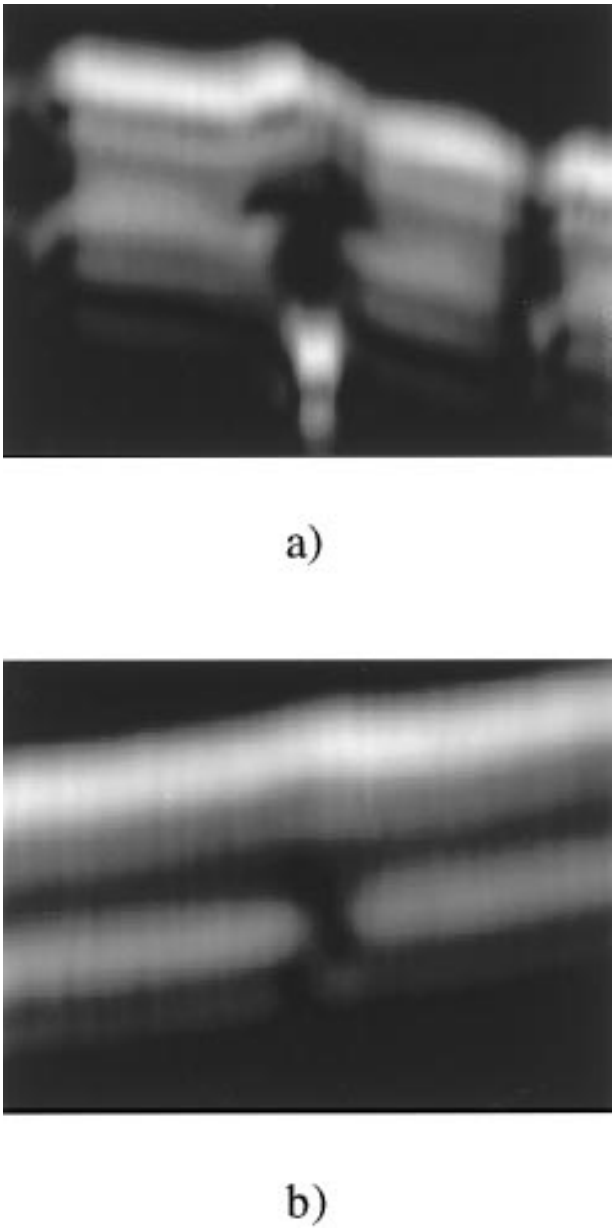

Fig. 6. Normal-incidence 17.3-MHz B-mode images of water-filled channels with (a) 220-μm and (b) 95-μm channel diameters (see Fig. 2 for their optical images). The reference needle marks are seen as shadow-like features on each side of the channel in (a). The image dimensions are 2.5 mm laterally (horizontally) and 0.7 mm axially (vertically).

acquisition), that is,

$$\mathrm{BAI} = \int_{t_1}^{t_2} |\mathrm{env}(\mathrm{RF}(t))|\, dt \tag{7}$$

where BAI denotes the backscattered amplitude integral and yields a single BAI value for each RF data acquisition (Fig. 4). The built-in MATLAB® function was used to process the Hilbert transformation. Because the Hilbert-transformed signal represents the envelope of the RF-signal amplitude, the BAI value is proportional to the square root of the backscattered energy. The integration

boundaries t_1 and t_2 define times prior to and beyond the locations of the sample's top and bottom surfaces, respectively, that is, the times between when the envelope of the received signal is nonzero (Fig. 4). Because the envelope of the signal is zero before and after the echoes occur from the sample, a wide time interval—for instance the depth of focus—may be chosen for the integration boundaries. Unlike conventional C-scan processing, which may include only a portion of the sample under investigation, the BAI time interval $t_2 - t_1$ includes the entire sample thickness. As long as the trilaminate material is flawless and its surfaces are smooth and parallel, the echoes from the sample surfaces and interfaces contribute a constant value to the integral. However, any imperfections within the material or on the surfaces can cause a variation in the total reflected signal received by the transducer and hence BAI-value variations are affected by alterations in the sample structure, such as channel defects, inclusions, delaminations, or surface wrinkles.

The entire acquired three-dimensional RF data set was used to process the BAI-mode image, that is, every 512-point RF data acquisition was processed by (7) to yield 4000 BAI values. The limits of integration in (7) were maintained constant. The two-dimensional (100×40) matrix of BAI values was then linearly interpolated (using the built-in MATLAB® function) by a factor of two in the direction perpendicular to the channel's long axis (30 μm/2) and by a factor of seven in the direction parallel to the channel's long axis (100 μm/7) to yield a 200×280 BAI-value matrix with a respective pixel size of 15.0 by 14.3 μm. Finally, the normalized matrix was displayed as a two-dimensional gray-scale map to yield a BAI-mode image. A BAI-mode image showed clearly not only a 95-μm channel defect, but also the reference needle marks, wrinkles, and delaminations (Fig. 7).

To provide a contrast descriptor for the BAI-mode image, it was observed that, for a normal-incidence BAI-mode image, the magnitude of the BAI value was lower within the region of the channel defect compared to the adjacent area (Fig. 7). This suggested that the total reflected echo signal, as assessed by (7), was lower in the region of the channel defect. This observation was further supported by the two weakly reflective reference marks (the dark-spot features—lower BAI values) and by the two strongly reflective delamination areas (the bright features—higher BAI values).

The BAI value also can be affected by varying the angle of incidence between sample surface and beam axis as observed by the horizontal surface wrinkling noted at the bottom of Fig. 7 (the faint horizontal features); this further suggested that data acquisition at an oblique angle of incidence (relative to the undisturbed plastic surface) could affect the BAI value and also the BAI-mode image appearance. Two BAI scans were acquired for two angles of incidence, viz., 0° and 6°; both scans traversed the same path across a 95-μm diameter water-filled channel defect (Fig. 8). A BAI scan is a one-dimensional display of, for this case, 100 normalized BAI values. Note that the BAI

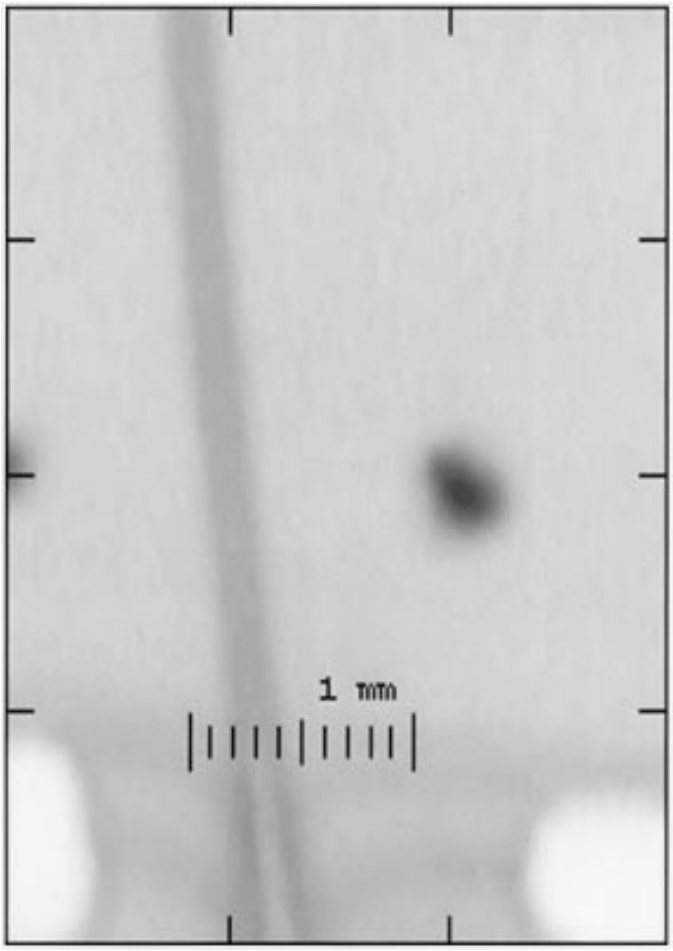

Fig. 7. Normal-incidence 17.3-MHz BAI-mode image of a 95-μm water-filled channel defect. The reference needle marks are seen as dark-spot features on each side of the channel. The bright spots on both lower corners are delaminations where the two trilaminate plastic layers were not sealed. The slightly darker horizontal bands near the bottom are surface wrinkles.

value is a minimum at the center of the channel defect for the normal-incidence case whereas there is an increase in the BAI value at the mid-channel location for the oblique-incidence case. The lateral shift of the detected channel location (in Fig. 8) is caused by the inclination of the transducer for the oblique incidence case.

An example of a contrast descriptor for channel defects in BAI-mode images can be defined as:

$$\Delta\text{BAI} = \text{BAI}_{\text{undisturbed}} - \text{BAI}_{\text{mid-channel}} \tag{8}$$

where $\text{BAI}_{\text{undisturbed}}$ is the unnormalized BAI value from the undisturbed region adjacent to the channel defect and $\text{BAI}_{\text{mid-channel}}$ is the unnormalized BAI value from the center location of the channel defect, and where $\text{BAI}_{\text{undisturbed}}$ and $\text{BAI}_{\text{mid-channel}}$ are calculated from (7). The quantity ΔBAI can be thought of as a measure of contrast in the BAI-mode image for the channel defect. The ΔBAI value can be either positive or negative. This appears to be dependent on the angle of incidence wherein the ΔBAI value is typically positive for normal incidence and negative for oblique incidence (Fig. 8). The dependence of ΔBAI as

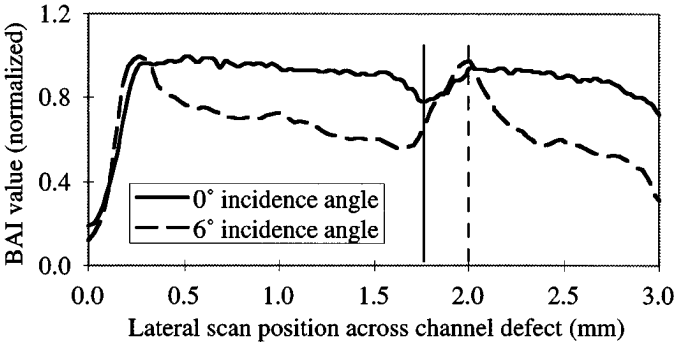

Fig. 8. BAI-scans at angles of incidence of (a) 0° and (b) 6° for the same 95 μm-diameter water-filled channel defect shown in Figs. 6 and 7. The solid vertical line indicates the channel location center for the 0° scan and the dashed vertical line indicated the channel location center for the 6° scan.

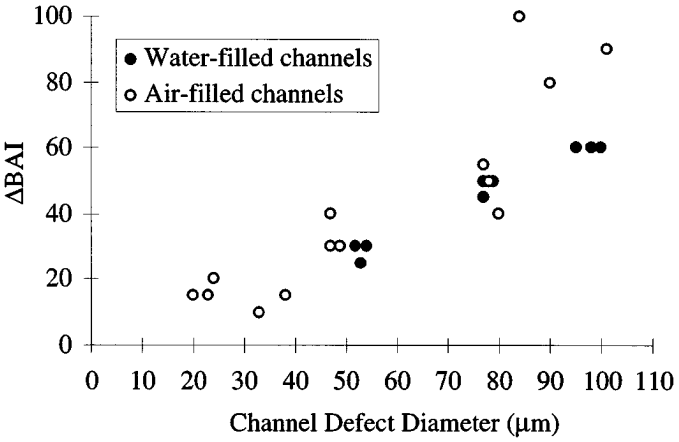

Fig. 9. The dependence of ΔBAI as a function of the channel defect diameter for data acquired at normal incidence with the 17.3 MHz source for both air-filled and water-filled channel defects.

a function of the channel diameter from normal-incidence BAI-mode images obtained with a 17.3-MHz transducer was evaluated for 9 water-filled and 14 air-filled channel defects (Fig. 9). From the BAI-mode image, the undisturbed region adjacent to the channel defect yielded the unnormalized $\mathrm{BAI}_{\mathrm{undisturbed}}$ value. Then the mean minimum unnormalized BAI value at the channel location was used to determine $\mathrm{BAI}_{\mathrm{mid\text{-}channel}}$ value.

A demonstration of image contrast variability as a function of data-acquisition angle of incidence is shown for a 10-μm air-filled channel defect (Fig. 10). The 17.3-MHz normal-incidence BAI-mode image clearly shows the two reference needle marks and the material imperfections, but the channel defect is weakly imaged [Fig. 10(b)]. However, the 17.3-MHz 7° BAI-mode image more clearly defines the channel defect [Fig. 10(c)]. Additionally, the 13.1-MHz 10° BAI-mode image visualizes the channel defect [Fig. 10(d)], but the channel defect at 13.1-MHz and 10° is not as well defined as for 17.3-MHz and 7° BAI-mode image.

V. Discussion

Conventional B-mode images were experimentally demonstrated to be inadequate for resolving channel-defect diameters less than the acoustic wavelength (Fig. 6). For normal-incidence conditions the echoes scattered from the channel defects were always partially or completely masked by the echoes generated from the top and bottom water-plastic interfaces. It was hypothesized that this was due to the much larger echo amplitudes from the top and bottom water-plastic interfaces which masked the much weaker echo amplitudes from the channel under conditions of a limited dynamic range and insufficient axial resolution, respectively. To compensate for this, the magnitude of the water-plastic interface echo amplitude had to be decreased relative to the channel echo amplitude. One approach to decreasing this ratio was to introduce the acoustic beam at an oblique angle of incidence, thereby decreasing the echo returned from the planar water-plastic interfaces without greatly affecting the echo return from the elliptically shaped channel. For small incidence angles ($\leq 10°$), the transmission coefficient across the water-plastic interfaces was not appreciably reduced from that at normal incidence. This would result in approximately the same echo amplitude return from the elliptically shaped channel while the echo amplitude return from the planar water-plastic interface was significantly reduced because the reflected echo was partially directed away from the transducer.

Even though oblique incidence angles in the range from 6° to 10° produced a significant improvement in B-mode image quality from that of the normal incidence case, B-mode images could not resolve channel-defects that were approximately 100 μm in diameter or smaller. However, the characteristic shadowing observation posterior to the channel location for channel diameters between about 50 and 100 μm in the B-mode images lead to the development of the new BAI-mode imaging technique. With the suggestion that the total reflected echo amplitude was affected in the region of the channel defect, a processing technique was investigated which mapped the two-dimensional distribution of reflected amplitude, that is, the BAI-mode imaging technique.

Contrast in the BAI-mode image appeared to be directly attributed to the strength of the reflected echo amplitude; this is currently under investigation [19], [20]. The reference needle marks were essentially holes through the sample which resulted in virtually no reflected signal; these reference marks appeared dark in the BAI-mode image (Fig. 7). On the other hand, delaminations (fabrication defects at the interface where the two plastics were bonded) in the sample resulted in a much greater reflected signal; these delaminations appeared bright in the BAI-mode image (Fig. 7). The weaker BAI values from the region of the channel defect provided contrast with the adjacent region, which allowed for the defect to be easily detected, and the contrast increased (ΔBAI value increased) as the channel diameter increased (Fig. 9). Considerable evaluation is still required to determine the cause underlying the apparent channel defect contrast effect, especially since ΔBAI is approximately the same for air-filled and water-filled channels smaller than about 80 μm in diameter. It is interesting

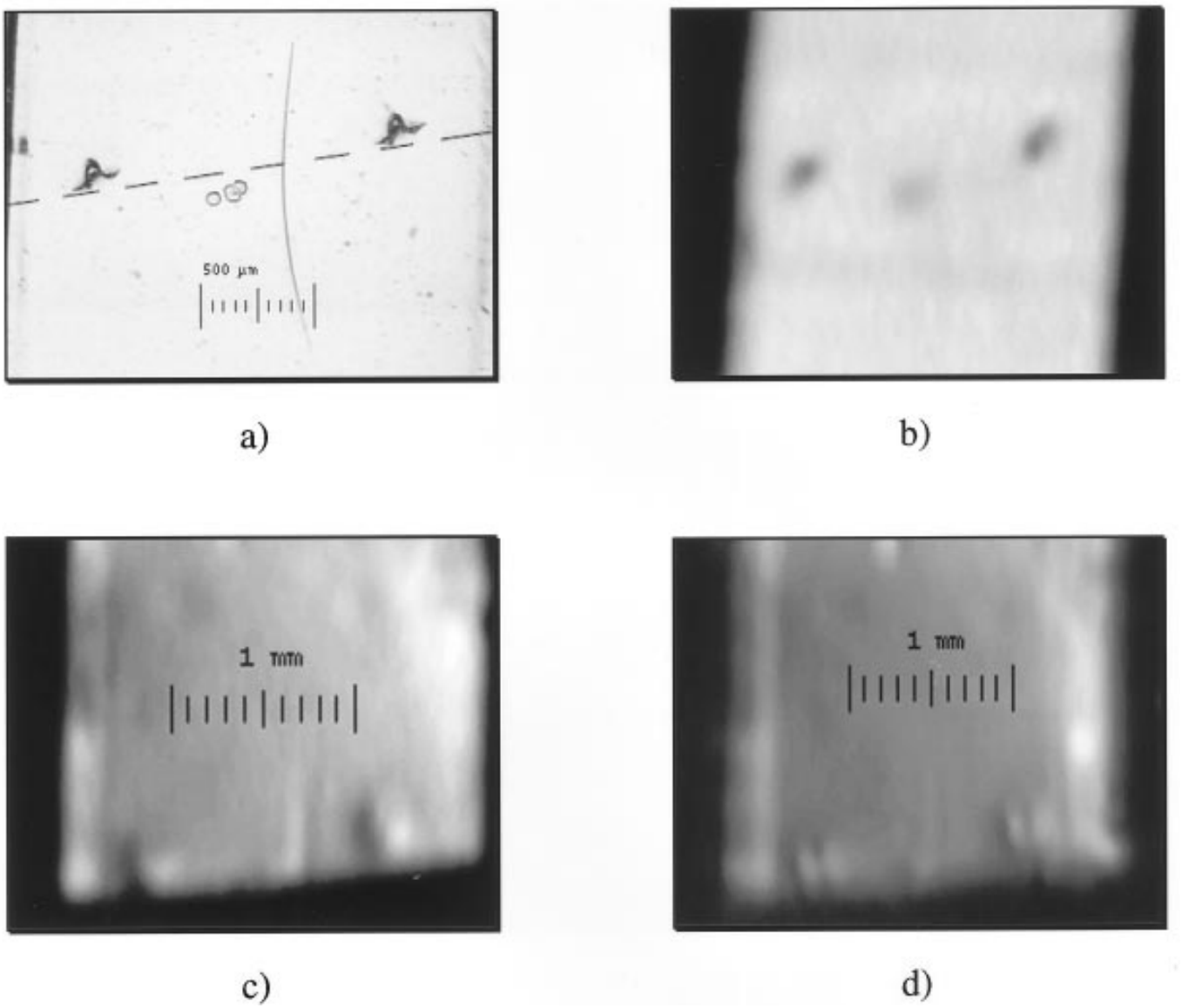

Fig. 10. (a) Light microscope image of a 10-μm air-filled channel defect, which is the slightly arched vertical line. The three roughly circular structures in the center are material imperfections, and the two dark regions are the reference needle marks. The dashed straight line indicates where the sample was cut for end-view light-microscopy evaluation. (b) 17.3 MHz, normal-incidence BAI-mode image prior to cutting in which the reference needle marks and material imperfections are clearly seen. (c) 17.3 MHz, 7° BAI-mode image, and (d) 13.1 MHz, 10° BAI-mode image after cutting with the cut-edge border the bottom boundary of the images.

to observe that a greater contrast appears to be the case for air-filled channel defects greater than about 85 μm compared to similar sized water-filled channels, that is, where $ka \approx 2$ or $a/\lambda \approx 1/\pi$.

The image features of the BAI-mode image changed significantly as a function of the angle of incidence (Fig. 10). For normal incidence, the decreased BAI value at the channel location (Fig. 8) is suggested to be caused by the decreased echo amplitude from the bottom water-plastic surface posterior to the channel location, presumably due to an interfering wave scattered from the channel which also produces a region of acoustic shadow in the B-mode images behind the channel. For oblique incidence, the increased BAI value at the channel location (Fig. 8) is suggested to be caused by increased echo amplitude from the channel without the strongly interfering signals from the water-plastic surfaces which are directed away from the transducer. The best BAI-mode image results appeared to be obtained when the angle of incidence was increased until only a small fraction of reflected echoes from the planar water-plastic surface were received by the transducer. Another interesting characteristic of the oblique-incidence BAI-mode images was its apparent ability to amplify topographical features of the sample surface.

The lateral extent of the channel defect appeared to be related to the field's spot size incident on the plastic sample. The normal-incidence BAI-mode image of a 95-μm water-filled channel defect exhibited a channel diameter of about 200 μm in the image (Fig. 7). This is consistent with a lateral resolution for the 17.3-MHz source of

174 μm (Table I). Thus, it should be noted that the observed channel size is larger than the actual channel defect size. Therefore, the BAI-mode imaging technique has potential for detecting channel defects, but it may be limited for characterizing the channel defect in term of its size.

The BAI-mode imaging technique has been shown to detect subwavelength ($\lambda_{\text{water}} \approx 86$–$113$ μm, $\lambda_{\text{plastic}} \approx 138$–$182$ μm) channel defects in plastic trilaminate. Air-filled and water-filled channel defects as small as 10 μm in diameter could be detected in the BAI-mode images at an ultrasonic center frequency of 17.3 MHz under oblique-incidence conditions. At 13.1 MHz, 10-μm air-filled and 20-μm water-filled channel defects appeared to be minimally detectable. Under normal-incidence conditions, the smallest detectable defect in BAI-mode images appeared to be about 25 μm in diameter.

BAI-imaging technology at 17.3 MHz appears to have the capability to detect channel defects in the 10-μm range regardless of whether low impedance (air) or high impedance (water) material resides within the channel defect; it is not known whether this is the smallest channel defect that can be imaged because the manufacturing of smaller defects represents considerable challenges. Combining this imaging capability with a reasonable depth of penetration and the ability to inspect opaque materials, BAI-technology has clear advantages compared to other nondestructive methods. At the ultrasonic frequencies evaluated, the capability of BAI-mode images already meets the requirements for safe food package inspection in terms of the critical channel size, that is, it can detect channel defects reliably for diameters less than 50 μm. Also, there is still the added potential to increase the ultrasonic frequency beyond that used in this study (i.e., up to, say, 100 MHz) to achieve an even better detection limit (i.e., < 10 μm) while, at the same time, maintaining a reasonable depth of penetration sufficient for common thicknesses of food packages (i.e., ≈ 0.2–0.4 mm).

Application of the results of this study will require improvements in the speed and spatial range of the scanning device used. Large commercial canning lines typically operate at speeds ranging from 250 cans per minute for large food cans, to more than 2600 cans per minute for beer and soft drinks. If the new types of packages are to be economically competitive, the inspection system should not represent the limiting factor on production speed. It may be possible to design a multitransducer or array-based unit which processes many units at production speed. There is and always will be a premium on increasing the speed and efficiency of the scanners used. Additionally, more information about the criticality of different types of defects and their attributes (path length, tortuosity, and positional variability) must be incorporated into the method in order to make the inspection device adaptable to real-world applications.

Acknowledgments

The authors would like to acknowledge the professional assistance with the sample validation by James F. Zachary, Department of Veterinary Pathobiology, University of Illinois.

References

[1] F. E. Long, "Flexible packages now withstand heat processing temperatures of foods," *Package Eng.*, vol. 7, no. 3, pp. 63–65, 69–72, 74, 76–77, 79–80, 1962.

[2] N. H. Mermelstein, "The retort pouch in the U.S.," *Food Technol.*, vol. 30, no. 2, pp. 28–37, Feb. 1976.

[3] A. F. Badenhop and H. P. Milleville, "Institutional size retort pouches," *Food Proc.*, vol. 41, no. 2, pp. 82–86, 1980.

[4] J. F. Steffe, J. R. Williams, M. S. Chinnan, and J. R. Black, "Energy requirements and costs of retort pouch vs can packaging system," *Food Technol.*, vol. 34, no. 9, pp. 39–44, 1980.

[5] United States Code of Federal Regulations. Published by the Office of the Federal Register. Superintendent of Documents, U. S. Government Printing Office, Washington, DC.

[6] R. A. Lampi, G. L. Schulz, T. Ciavarani, and P. T. Burke, "Performance and integrity of retort pouch seals," *Food Technol.*, vol. 30, no. 2, pp. 38–48, Feb. 1976.

[7] C. L. Harper, B. A. Blakistone, J. B. Litchfield, and S. A. Morris, "Developments in food packaging integrity testing," *Food Technol.*, vol. 6, no. 10, pp. 336–340, 1995.

[8] J. E. Gilchrist, B. S. Dhirendra, C. R. Dave, and W. D. Roger, "Leak detection in flexible retort pouches," *J. Food Prot.*, vol. 52, no. 6, pp. 412–415, June 1989.

[9] D. Jarmon, B. Farahbakhsh, and R. Herzig, U.S. Patent 5,343,042, "Ultrasonic inspection of seal integrity of bond lines in sealed containers," Dec. 13, 1994.

[10] D. T. Maunder, J. F. Folinazzo, and J. J. Killoran, "Bio-test method for determining integrity of flexible packages of shelf-stable foods," *Food Technol.*, vol. 22, no. 5, pp. 615–618, May 1968.

[11] L. Axelson, S. Cavlin, and J. Nordstrom, "Aseptic integrity and microhole determination of packages by electrolytic conductance measurement," *Packaging Technol. Sci.*, vol. 3, pp. 141–162, 1990.

[12] J. W. Szczeblowski and F. J. Rubinate, "Integrity of food packages," *Modern Packaging*, vol. 38, no. 10, pp. 131–134, 1965.

[13] A. A. Safvi, H. J. Meerbaum, S. A. Morris, C. L. Harper, and W. D. O'Brien, Jr., "Acoustic imaging of defects in flexible food packages," *J. Food Prot.*, vol. 60, pp. 309–314, Mar. 1997.

[14] A. R. Selfridge, "Approximate material properties in isotropic materials," *IEEE Trans. Sonics Ultrason.*, vol. SU-32, no. 3, pp. 381–395, May 1985.

[15] R. E. Bolz and G. L. Tove, *Handbook of Tables for Applied Engineering Science*. Boca Raton, FL: CRC Press, 1981.

[16] K. Raum and W. D. O'Brien, Jr., "Pulse-echo field distribution measurement of high-frequency ultrasound sources," *IEEE Trans. Ultrason., Ferroelect., Freq. Contr.*, vol. 44, no. 4, pp. 810–815, July 1997.

[17] B. G. Lucas and T. G. Muir, "The field of a focusing source," *J. Acoust. Soc. Amer.*, vol. 72, no. 4, pp. 1289–1296, 1982.

[18] G. S. Kino, *Acoustic Waves: Devices, Imaging, and Analog Signal Processing*. Englewood Cliffs, NJ: Prentice-Hall, 1987.

[19] A. Ozguler, S. A. Morris, and W. D. O'Brien, Jr., "Evaluation of defects in seal region of food packages using the backscattered amplitude integral (BAI) technique," *Proceedings of the 1997 IEEE Ultrasonics Symposium* (in press).

[20] C. H. Frazier, A. Ozguler, S. A. Morris, and W. D. O'Brien, Jr., "High-contrast images of defects in material seals," *Proceedings of the 1997 IEEE Ultrasonics Symposium* (in press).

[21] W. D. Wilson, "Speed of sound in distilled water as a function of temperature and pressure," *J. Acoust. Soc. Amer.*, vol. 31, pp. 1067–1072, 1959.

Kay Raum was born in Halle/Saale, Germany, on March 1, 1972. He received his Vordiplom in Physics from the Martin Luther University of Halle-Wittenberg in 1993. From 1995–1996 he was with the Bioacoustics Research Laboratory at the University of Illinois at Urbana-Champaign as a Visiting Scholar. Currently he is pursuing his Diplom degree in Physics from the Martin Luther University of Halle-Wittenberg.

His interests are in high frequency acoustic imaging and characterization of biological tissues.

Ayhan Ozguler was born in Ankara, Turkey, in 1968. He earned a B.S. degree from the Food Engineering department at the Middle East Technical University in Ankara, Turkey, in 1991, and received a M.S. degree from the Food Science and Human Nutrition Department at the University of Illinois, Urbana-Champaign in 1995. Currently he is enrolled in the Ph.D. program of the same department at the University of Illinois, and has been employed as a research assistant since 1994.

He was awarded the government scholarship of Turkey to pursue master and Ph.D. degrees in the area of food packaging in the US in 1993.

Scott A. Morris received the B.S., M.S., and Ph.D. degrees in 1981, 1987, and 1992 from Michigan State University.

While employed at Michigan State University, he worked with a variety of problems related to the packaging industry. Development of an experimental permeation modeling technique utilizing a combination of numerical modelling, optical measurement techniques, and laboratory analytical testing methods. Microwave cooking of frozen and shelf-stable foods, and the redesign of their related package systems. Improved shipping designs for retortable-pouch packaging systems. Development of chromatographic methods for the evaluation of volatile extractables from packaging materials. Determination of oxygen-barrier requirements of products that had been previously packaged in impermeable cans, and the evaluation of the suitability of producer-supplied polymeric replacements. Development of a research program in conjunction with a major packaging corporation, to test the ability of their 2-liter aseptic package to survive shipping and distribution. A survey of the state-of-the-art of packaging in the United States, and significant trends in the technical and economic aspects of the packaging industry commissioned by the Congressional Office of Technical Assessment (OTA). Investigating the relationship of package design to the effects of shock, vibration and compression on fresh and controlled-atmosphere-stored produces gaseous metabolic by-products.

Since 1992 he has been at the University of Illinois as an assistant professor in the departments of Food Science and Human Nutrition and Agricultural Engineering. He currently is developing a packaging research and teaching program. Current research projects within the program include: leak detection in shelf-stable food packages using high-frequency ultrasound, predictive modeling of package-structure permeation properties; static and dynamic structural modeling for design strength, and material-use optimizaton; packaging line efficiency optimization; product quality degradation from mechanical input and thermal variation; time-dependent material properties from stress-strain histories using recursive finite element algorithms; and microwave energy dispersion in food packages.

Dr. Morris is a member of the executive committee of the Institute of Food Technologists (IFT) Food Packaging Division, a member of the American Society of Agricultural Engineers (ASAE), Society of Professional Engineers (SPE), Institute of Packaging Professionals (IoPP), American Society for Engineering Education (ASEE), Pi Kappa Gamma, and Gamma Sigma Delta.

William D. O'Brien, Jr. (S'64–M'70–SM'79–F'89) received the B.S., M.S., and Ph.D. degrees in 1966, 1968, 1970, from the University of Illinois, Urbana-Champaign.

From 1971 to 1975 he worked with the Bureau of Radiological Health (currently the Center for Devices and Radiological Health) of the U.S. Food and Drug Administration. Since 1975, he has been at the University of Illinois, where he is a Professor of Electrical and Computer Engineering and of Bioengineering, College of Engineering, and Professor of Bioengineering, College of Medicine. He is the Director of the Bioacoustics Research Laboratory and the Program Director of the NIH Radiation Biophysics and Bioengineering in Oncology Training Program. His research interests involve the many areas of acoustics and ultrasound, including spectroscopy, risk-assessment, biological effects, tissue characterization, dosimetry, blood-flow measurements, acoustic microscopy, and imaging. He has published more than 180 papers.

Dr. O'Brien is Editor-in-Chief of the *IEEE Transactions on Ultrasonics, Ferroelectrics, and Frequency Control*. He is a Fellow of the Institute of Electrical and Electronics Engineers (IEEE), the Acoustical Society of America (ASA), and the American Institute of Ultrasound in Medicine (AIUM), and he is a Founding Fellow of American Institute of Medical and Biological Engineering. He was recipient of the IEEE Centennial Medal (1984), the AIUM Presidential Recognition Awards (1985 and 1992), the AIUM/WFUMB Pioneer Award (1988), the IEEE Outstanding Student Branch Counselor Award (1989), and the AIUM Joseph H. Holmes Basic Science Pioneer Award (1993). He has been President (1982–1983) of the IEEE Sonics and Ultrasonics Group (currently the IEEE UFFC Society), Co-Chairman of the 1981 IEEE Ultrasonic Symposium, and General Chairman of the 1988 IEEE Ultrasonics Symposium, President of the AIUM (1988–1991), and Treasurer of the World Federation for Ultrasound in Medicine and Biology (1991–1994). He is the 1997–1998 IEEE UFFC Society's Distinguished Lecturer.